Int. J. Electrochem. Sci., 15 **(2020)** 11356 – 11370, doi: 10.20964/2020.11.27

International Journal of ELECTROCHEMICAL SCIENCE
www.electrochemsci.org

Study on the Effect of the Pre-treatment Temperature on $Li_{1.2}Mn_{0.54}Ni_{0.13}Co_{0.13}O_2$ Cathode Material

Yi Jin[1,†], Chen Hu[1,†], Cheng Chen[2,†], Dandan Sun[2], Chunyu Du[2,], Jiyuan Jian[2], Geping Yin[2]*

[1] State Key Laboratory of Operation and Control of Renewable Energy & Storage Systems, China Electric Power Research Institute, Beijing 100192, China
[2] MIIT Key Laboratory of Critical Materials Technology for New Energy Conversion and Storage, School of Chemistry and Chemical Engineering, Harbin Institute of Technology, Harbin 150001, China
† These authors contributed equally.
*E-mail: cydu@hit.edu.cn

Received: 14 July 2020 / *Accepted:* 26 August 2020 / *Published:* 30 September 2020

Lithium-rich manganese-based cathode materials (LMO) have been considered the most promising candidate materials for next-generation lithium-ion batteries due to their high theoretical specific capacity (>300 mAh g^{-1}). However, the low initial Coulombic efficiency, significant capacity fading and poor rate capability have restricted their commercial application. In particular, the synthesis process of lithium-rich materials plays a decisive role in their structure and electrochemical performance. This paper mainly studies the effect of the pre-treatment temperature on the structure and performance of lithium-rich materials. The calcination temperature affects the performance of the lithium-rich material by changing the structure of the metal oxide (MO). Consequently, 600°C-LMO has better cycling stability and rate performance than 700℃-LMO and 500℃-LMO. 600℃-LMO delivers a high initial charge capacity of 252 mAh g^{-1} with a large initial Coulombic efficiency of 81.4% at 0.1 C. After cycling 50 times, large and stable discharge capacities of 229 mAh g^{-1} can be obtained. Both XRD and SAED characterize the presence of a spinel structure in 600℃-LMO, and the heterogeneous lithium-rich material shows excellent cycling stability and rate performance.

Keywords: Lithium-ion battery, Li-rich, cathode, pre-treatment temperature, spinel phase

1. INTRODUCTION

With the widespread application of electric vehicles and portable devices, higher requirements have been placed on the energy density and service life of lithium-ion batteries[1, 2]. Since the energy density of the anode material is much greater than that of the positive electrode, the positive electrode material has become the "short board of the barrel"—the lower limit of the energy density of the lithium-ion battery depends on the cathode material. To increase the energy density, we must

continuously upgrade the positive electrode material[3-5]. However, the actual specific capacities of the commercialized lithium-ion battery cathode materials ($LiCoO_2$, $LiFePO_4$, $LiNi_{0.8}Co_{0.1}Mn_{0.1}O_2$, $LiMn_2O_4$, etc.) are all below 200 mAh g^{-1}[6-8]. Lithium-rich manganese-based cathode materials ($xLi_2MnO_3 \cdot (1-x)\ LiMO_2$, where M = Mn, Ni, Co, etc.) have been considered the most promising candidate materials for next-generation lithium-ion battery cathode materials due to their excellent reversible specific capacity, good cycling stability and thermal stability, low price, and environmental friendliness[9-11]. Nevertheless, they have a variety of deficiencies, such as low efficiency, poor rate and poor cycling performance the first time, which limit the application of lithium-rich manganese-based solid solution cathode materials[12, 13]. Numerous approaches have been exploited to improve the electrochemical performance, such as coating, element doping, and heterostructure construction[14-20].

In particular, the synthesis method plays a decisive role in the structure and electrochemical performance[21, 22]. To date, researchers have conducted much research on the synthesis of lithium-rich manganese-based solid solution cathode materials, including via co-precipitation[23, 24], a high-temperature solid-phase method[25], sol-gel method[26, 27], and hydrothermal method[28]. The high-temperature solid-phase method involves preparing the precursor by mixing the reactants uniformly according to the stoichiometric ratio and directly obtaining the lithium-rich cathode material after grinding and high-temperature calcination, which is convenient. First, the precursor material is prepared by a co-precipitation method with good reproducibility, which is suitable for large-scale production and can achieve uniform mixing at the atomic level and realize a highly compact spherical precursor material with a micro-nano-structure[29]. Then, the lithium-rich manganese-based cathode material is prepared by pre-treatment and calcination with lithium.

The pre-treatment process mainly decomposes the carbonate precursor into CO_2 and transition metal oxides[30]. Changing the calcination temperature or atmosphere affects the valence state and phase composition of the metal oxide, which will affect the diffusion and migration process of Li^+ during calcination with lithium, leading to differences in the final structure and electrochemical performance of the material[21, 30]. Therefore, it is necessary to explain the corresponding relationship between the different conditions during the pre-treatment process and the material properties. This will help us further optimize the electrochemical performance of the material by changing the pre-firing process conditions.

In this paper, a lithium-rich manganese-based solid solution cathode material was prepared by changing the pre-firing temperature while maintaining the same atmosphere, temperature and atmosphere for calcination with lithium. By comparing the structural differences between the samples prepared with different pre-treatment temperatures, the mechanism of the effect of the pre-treatment temperature on the electrochemical performance of lithium-rich cathode materials was studied and elaborated.

2. EXPERIMENT

2.1 Material preparation

The $Li[Li_{0.2}Mn_{0.54}Ni_{0.13}Co_{0.13}]O_2$ (labelled LMO) sample was successfully synthesized via a

high-temperature solid-state reaction. A 2 mol L^{-1} metal salt solution (Mn:Ni:Co=4:1:1) and certain concentrations of sodium carbonate (Na_2CO_3) and ammonia solution ($NH_3 \cdot H_2O$) were combined. A peristaltic pump and an acidity meter were used to control the feed rate and pH value during the reaction. The carbonate precursor of the spherical lithium-rich cathode material ($Mn_{0.66}Ni_{0.17}Co_{0.17}CO_3$) was prepared by reaction at a suitable reaction temperature and stirring speed for 12 h.

Then, the carbonate precursor was pyrolyzed into CO_2 and metal oxide (MO) materials via firing in air for 5 h at different temperatures (500℃, 600℃, 700℃). Pre-burned MO and $LiOH \cdot H_2O$ were mixed with Li/M (M=Mn, Ni, Co) at a molar ratio of 1.2:1, then calcined at 950°C for 12 h in air and quenched to room temperature naturally. Lithium-rich materials pre-treatment at different temperatures (500℃-LMO, 600℃-LMO,700℃-LMO) were synthesized.

2.2 Material characterization

The morphology and chemical composition of the material were tested and analysed by FEI QUANTA 200 FEG field emission scanning electron microscopy technology, and the working voltage was 20 kV. The crystal structure of the prepared material and the structural changes of the material after cycling were studied by Panalytical Empyrean powder X-ray diffraction, and the XRD test results were refined by GSAS software to calculate the cell parameters and other crystal parameters. The target of the used XRD test instrument was a Cu target, the diffraction angle was 10°~80° for data collection, and the step scanning method was used. A Tecnai G2F30 transmission electron microscope was used to analyse the structure of the material. At the same time, this type of transmission equipment was equipped with X-ray energy spectrum analysis (EDX), which can be used to analyse the element distribution of the material. It uses field emission, and the working voltage was 300 kV. PHI X-ray photoelectron spectroscopy was used to determine the valence state and relative content of elements in the material, with Al-Kα as the excitation source.

2.3 Electrochemical measurements

The prepared lithium-rich material was made into positive electrodes by using a ratio of active material (LMO):conductive agent (Super P):binder (5% PVDF) of 8:1:1. A lithium metal sheet was used as the negative electrode, the electrolyte was a commercial electrolyte or a prepared electrolyte ($LiPF_6$ dissolved in 50 vol% ethylene carbonate (EC) and 50 vol% dimethyl carbonate (DMC)), and the separator was a 2325-type polypropylene film. The CR2025 button battery was assembled in a super clean glove box for all electrochemical testing.

A Neware battery testing system was applied to carry out the galvanostatic charge/discharge measurements between 2.0 and 4.6 V (vs Li^+/Li) at different current rates (1 C=300 mA g^{-1}). Electrochemical impedance spectroscopy (EIS) was performed using a PARSTAT 2273 electrochemical workstation, the frequency range was 1 mHz~1 MHz, and the battery state of charge was 4.3 V in the charged state.

3. RESULTS AND DISCUSSION

3.1 Physical characterization

The morphologies of 500℃-LMO, 600℃-LMO, and 700℃-LMO are shown in Fig. 1. From Fig. 1(a)~(c), we can clearly observe that the surface morphology and particle size of the lithium-rich materials prepared after pre-treatment at 500, 600, and 700°C are similar, and the primary particles are closely packed, indicating that the macro-morphology of the lithium-rich materials has not changed after changing the pre-treatment temperature.

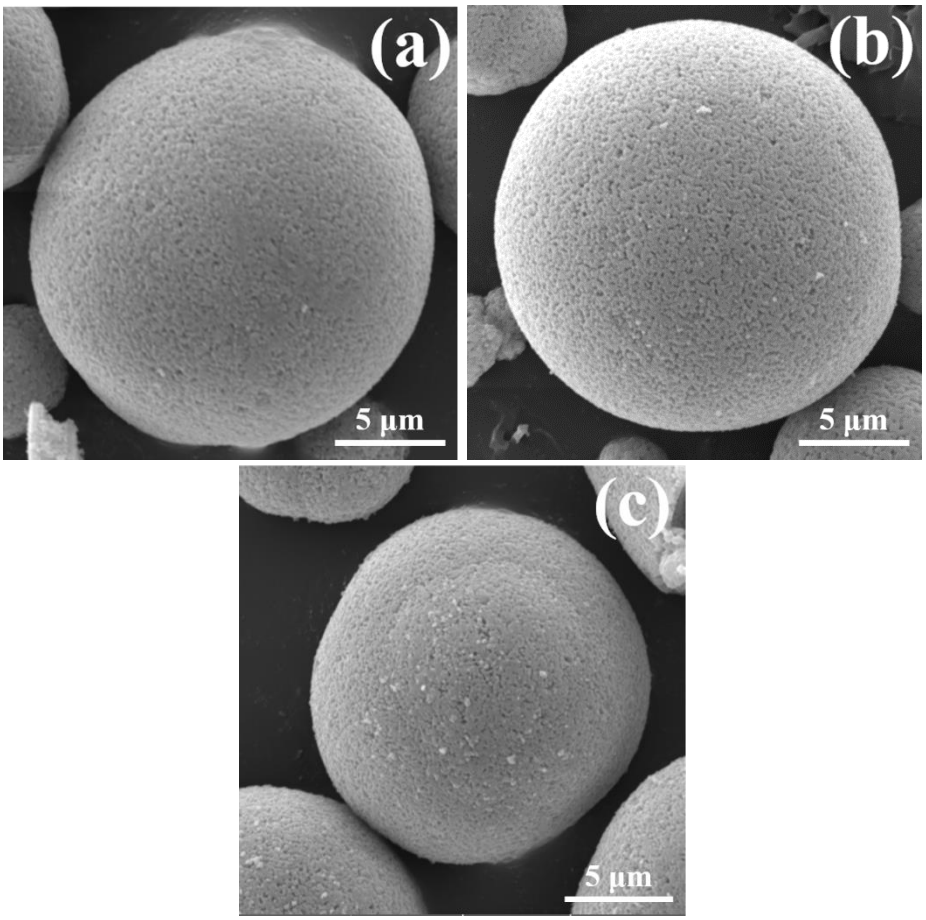

Figure 1. SEM images of (a) 500℃-LMO, (b) 600℃-LMO, and (c) 700℃-LMO

The crystalline structural data of these samples were detected by powder XRD diffraction. Fig. 2 (a) shows that the MO diffraction peaks for the sample pre-treatment at 600℃ mainly belong to the Mn_3O_4 and $CoMnO_3$ phases corresponding to the tetragonal spinel and hexagonal layered crystal structures, respectively. The MO diffraction peaks for the sample pre-treatment at 500℃ correspond to Mn_3O_4, and there are also some miscellaneous peaks, which belong to CoO and $(NiO)_{0.5}(MnO)_{0.5}$, corresponding to monoclinic and cubic crystal structures, respectively. The peaks of 700℃-MO could be attributed to Mn_2O_3 and $CoMnO_3$ belonging to the orthorhombic system and the hexagonal layered structure. Different phase compositions appear in the metal oxides calcined at different temperatures

because the transition metal ions are oxidized to different degrees at different temperatures. When the calcination temperature is 700℃, the temperature is the highest, and the ion valence state of the transition metal oxide is a high valence state. When the calcination temperature is 600℃, the valence state of the transition metal ions in the transition metal oxide is a mixed valence state, and when the calcination temperature is 500℃, the valence state of the transition metal ions in the transition metal oxide is a low valence state. The above results indicate that due to the different calcination temperatures, the valence state of the transition metal ions in the corresponding metal oxide changes, which affects the phase composition and crystal structure of MO, consistent with the experimental design results.

Fig. 2 (b) displays the XRD patterns of 500℃-LMO, 600℃-LMO, and 700℃-LMO. The diffraction peaks of the three sets of lithium-rich materials correspond to the diffraction peaks of the hexagonal layered structure and the monoclinic layered structure, and the superlattice structure of the Li_2MnO_3 phase appears between 20° and 25°, indicating that lithium-rich manganese-based solid solution cathode materials have been prepared under the different calcination atmospheres[31-33]. However, the lithium-rich material pre-treatment at 600℃ shows small intensity peaks at 37.8°, 58.3°, 76.8° and 80.9° corresponding to spinel $LiMn_2O_4$ diffraction peaks. This may be due to the presence of Mn_3O_4 in the pre-treatment MO, and a spinel phase structure is formed after lithium-mixed sintering. The presence of the spinel structure is beneficial for improving the electrochemical performance of the material[34].

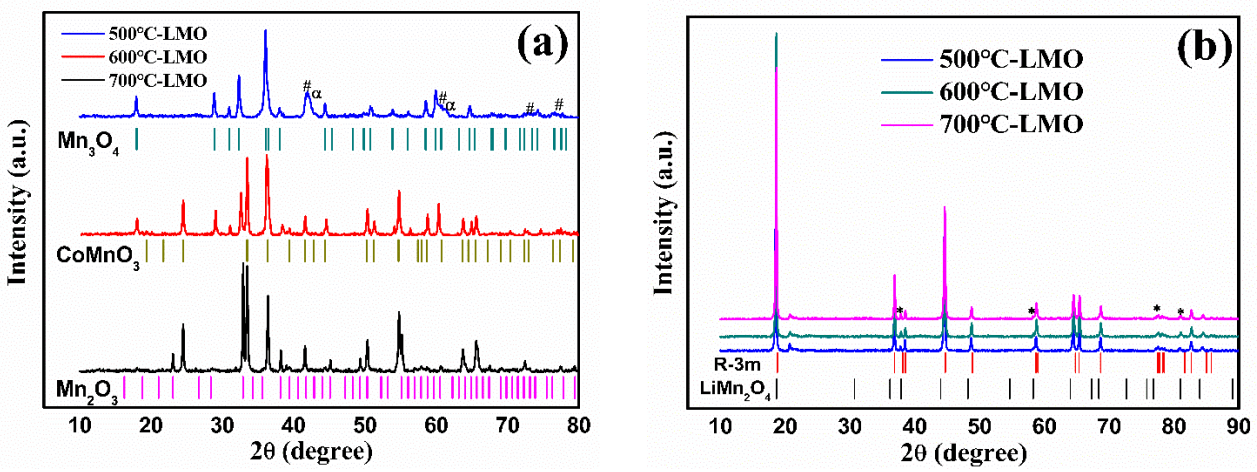

Figure 2. XRD patterns of (a) MO and (b) LMO, where α, #, and * correspond to the peaks of CoO, $(NiO)_{0.5}(MnO)_{0.5}$, and $LiMn_2O_4$.

The results of the unit cell parameters calculated through refinement are shown in Table 1, where c is the interlayer spacing for intercalation into and deintercalation from the layered material, and its size corresponds to the difficulty of intercalation and deintercalation for the material. The larger the value is, the better the electrochemical performance of the material. c/a is an important parameter of the hexagonal layered structure in the reaction material, and the three groups of materials are typical layered structures based on a comparison of the c/a values. When the crystalline material changes from the cubic structure to the hexagonal layered structure, this will be accompanied by an increase in the

cell parameter c— deformation along the c axis. The higher the c/a value is, the more obvious the hexagonal layered structure. I(003)/I(104) can reflect the degree of ion mixing in lithium-rich materials to a certain extent. Generally, when the ratio is greater than 1.2, the ion mixing is smaller. The ion mixing in layered materials is mainly the mixing of Li^+ and Ni^{2+}, mainly because the ion radii of Li^+ and Ni^{2+} are very similar. The I(003)/I(104) ratios of these three groups of materials are all greater than 1.2, and the ratio is the largest for the sample pre-treatment at 600℃.

Table 1. Refinement results of the lattice parameters of lithium-rich materials pre-treatment at different temperatures

	a=b (Å)	C (Å)	c/a	V (Å^3)	I(003)/I(104)
500℃-LMO	2.866512	14.215948	4.9593	116.81089	1.448
600℃-LMO	2.854962	14.251395	4.9918	116.16038	1.682
700℃-LMO	2.854444	14.245578	4.9906	116.07084	1.661

To further confirm the existence of the spinel phase structure in 600℃-LMO, SAED characterization of the 600℃-LMO material was carried out. Fig. 3 (b) displays the monoclinic layered structure diffraction pattern. The two darker spots in the white circle appear in pairs, corresponding to the superlattice lattice in the 600℃-LMO material.

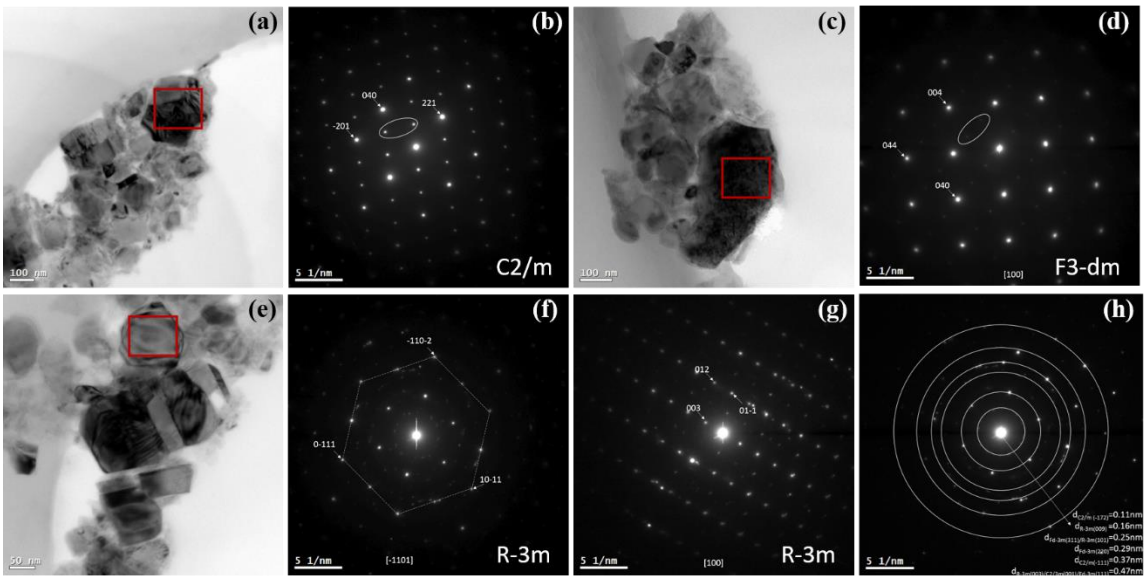

Figure 3. SAED map at different positions of the 600℃-LMO material

The selected area electron diffraction patterns in Fig. 3 (d) and 3 (f, g) are typical cubic spinel structure and hexagonal layered structure patterns, respectively. Fig. 3 (h) shows the selective area

electron diffraction pattern of the composite structure. It can be observed that 600℃-LMO has a hexagonal layered-monoclinic layered-cubic spinel composite structure by measuring the distance from different diffraction circles to the central diffraction point of the spinel composite structure, which corresponds to the above XRD test results. This heterogeneous composite structure can give full play to the high capacity of the layered material and the high rate performance of the spinel material, thereby greatly improving the electrochemical performance of the material. The distribution of the spinel of the composite structure prepared by changing the pre-treatment temperature should be distributed from the inside to the outside, which is different from the surface spinel structure formed by ordinary surface modification.

3.2 Electrochemical performance

To evaluate the electrochemical performance of all samples, the initial charge-discharge curves at a rate of 0.1 C and rate performance curves of 500℃-LMO, 600℃-LMO and 700℃-LMO between 2.0 and 4.6 V are shown in Fig. 4 (a). The lithium-rich materials prepared at different temperatures have similar charging curves at a current density of 0.1 C during the initial charge process, including a ramp-up curve below 4.4 V and a plateau at 4.5 V, which is usually ascribed to activation of Li_2MnO_3. However, the plateau length of the 700℃-LMO material is much shorter than that of the other two groups of materials, indicating that the activation reaction of the lithium-rich material Li_2MnO_3 pre-treatment at 700℃ is suppressed. Among the three groups of materials, 600℃-LMO shows the highest initial discharge capacity of 252 mAh g^{-1} at a current density of 0.1 C, and the initial cycle Coulombic efficiency is 81.4%, while the specific discharge capacities of the 500℃-LMO and 700℃-LMO materials are only 224 and 136.3 mAh g^{-1}, respectively, and the initial Coulombic efficiencies are only 73.8% and 56.1%, respectively. The layered-spinel heterostructured lithium-rich material pre-treatment at 600℃ exhibits better initial specific capacity and Coulombic efficiency, which is mainly because the spinel provides many three-dimensional Li transport pathways to promote Li transport and the occurrence of electrochemical reactions. At the same time, the reduction in the irreversible capacity loss may be due to the change in the interface structure of the lithium-rich material prepared by calcination at different temperatures. Fig. 4 (b) shows the rate performance of the three samples at different rates at room temperature from 2 V to 4.6 V. Distinctly, the 600℃-LMO cathode delivers the best rate performance compared to the 500℃-LMO and 700℃-LMO cathodes. The specific discharge capacities of the 500℃-LMO, 600℃-LMO, and 700℃-LMO materials are 143, 257, and 226 mAh g^{-1} at a current density of 30 mA g^{-1}. When the current density increases to 300 mA g^{-1}, the 600℃-LMO material still has a current density of 183 mAh g^{-1}, while the 500℃-LMO and 700℃-LMO materials only have values of 17 and 148 mAh g^{-1}. At 1000 mA g^{-1}, the specific discharge capacity of the 600℃-LMO material is 127 mAh g^{-1}, which is 45 mAh g^{-1} higher than that of the 700℃-LMO material, and the 500℃-LMO material discharge capacity is close to zero. For 600℃-LMO, the improvement of the rate capability may be attributed to the presence of the spinel phase, which provides three-dimensional transport channels in the layered material, ensuring the rapid intercalation and decoupling of Li^+ with large performance enhancement[35]. The cycling performance comparison between 600℃-LMO and

other cathode materials of lithium-ion batteries is shown in Table 2. The former exhibits high initial capacity and good cycling performance.

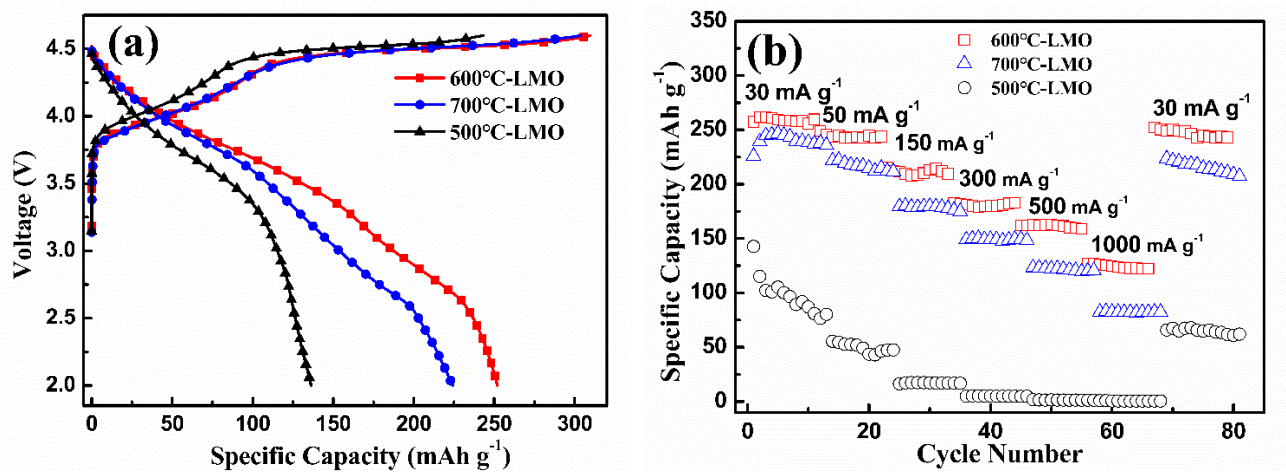

Figure 4. (a) Initial charge and discharge curves of 500℃-LMO, 600℃-LMO and 700℃-LMO at 0.1 C, and (b) rate performance curves

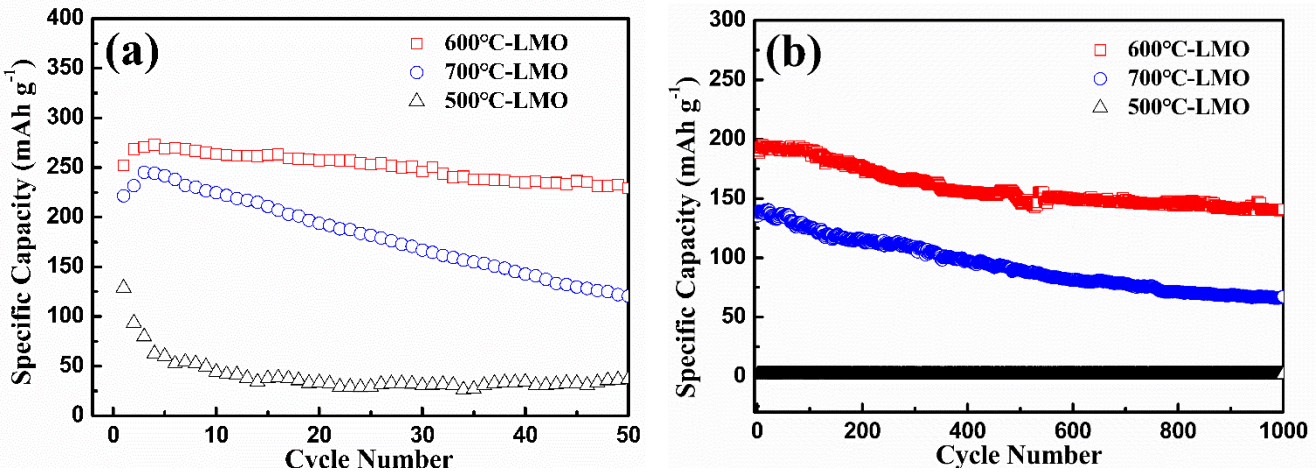

Figure 5. Cycling performances of 500℃-LMO, 600℃-LMO and 700℃-LMO materials at (a) 0.1 C and (b) 1 C

To compare the cycling stability of the materials synthesized under different calcination atmospheres, constant current charge and discharge tests were conducted at 0.1 C and 1 C, respectively. As displayed in Fig. 5 (a), after 50 cycles of 0.1 C, the specific discharge capacity of the 600℃-LMO material is 229 mAh g^{-1} with a capacity retention rate of 91.4%. By contrast, the specific discharge capacities of the 500℃-LMO and 700℃-LMO materials are only 37 and 121 mAh g^{-1}, and the capacity retention rates are 54.5% and 28.5%, respectively. Fig. 5 (b) shows the cycling performance curves of the three groups of materials at 1 C. As expected, the discharge capacity retention of 600℃-LMO reveals a visible improvement, with a capacity retention of 82% after 50 cycles at 1 C and a maximum discharge capacity of 189 mAh g^{-1}. After 1000 cycles at 1 C, the

discharge capacity of the 600℃-LMO material can still reach 141 mAh g^{-1}. By comparison, the specific discharge capacity retention of the 700℃-LMO material after 1000 cycles is less than 50%, and the specific discharge capacity of the 500℃-LMO material is almost 0 at 1 C.

Table 2 Cycling performance comparison with other cathodes

Cathode	1st discharge capacity (mAh/g)	Cycling capacity at 25℃				**Ref.**
		Current density (mA/g)	Cycle number	Reversible capacity (mAh/g)	Capacity retention (%)	
$LiCoO_2$	174.7/0.1 C	37	100	169.4	97	[36]
$LiNi_{0.8}Co_{0.1}Mn_{0.1}O_2$	202/0.1 C	270	100	120.3	65.74%	[7]
Li-rich NMC	243/0.1 C	270	50	96	87%	[37]
$LiFePO_4$	163.3/0.2 C	170	100	158	99.63%	[6]
LMCrR@LP	275.5/0.1C	150	200	154.8	76.5%	[38]
600℃-LMO	257/0.1 C	300	200	174	94%	This work

Table 3. Comparison of the negative voltage shifts and specific discharge capacities of 500℃-LMO, 600℃-LMO and 700℃-LMO materials

	Voltage shift after 50 cycles at 0.1 C (mV)	Specific discharge capacity in 5/10/20/30/40/50 th cycles (mAh/g)	Specific discharge capacity in 5/10/20/30/40/50th cycles from 3.5-4.6 V (mAh/g)
500℃-LMO	350	60,44,33,30,34,37	22,12,10,9,9,7
600℃-LMO	50	269,263,257,246,235,229	118,107,97,89,82,75
700℃-LMO	100	242,225,194,167,143,121	96,83,64,52,43,34

Meanwhile, the voltage decay of lithium-rich materials is an important issue that puzzles researchers. Fig. 6 shows the charge-discharge curves of the 500℃-LMO, 600℃-LMO and 700℃-LMO materials in the 5th, 10th, 20th, 30th, 40th and 50th cycles (Fig. 6 (a, c, e)) and the corresponding dQ/dV plots (Fig. 6 (b, d, f)). Table 3 shows the comparison of the negative voltage shift and specific discharge capacity of these materials after 50 cycles at 0.1 C. From the data in the table, we can see that for 500℃-LMO, 600℃-LMO and 700℃-LMO, the capacity was attenuated by 14.9% 38.3% and 50%, respectively. Fig. 6 (b, d, f) shows the corresponding differential capacity curves. Taking 600℃-LMO as an example, there are three peaks in the discharge process at 4.3 V, 3.75 V, and 3.2 V, corresponding to the reduction reactions of Ni, Co, and Mn. As the cycling progresses, the

reduction peak of Mn begins to negatively shift and gradually widens, which is mainly due to the voltage decay caused by the phase transition of the internal structure of the material during the cycling.

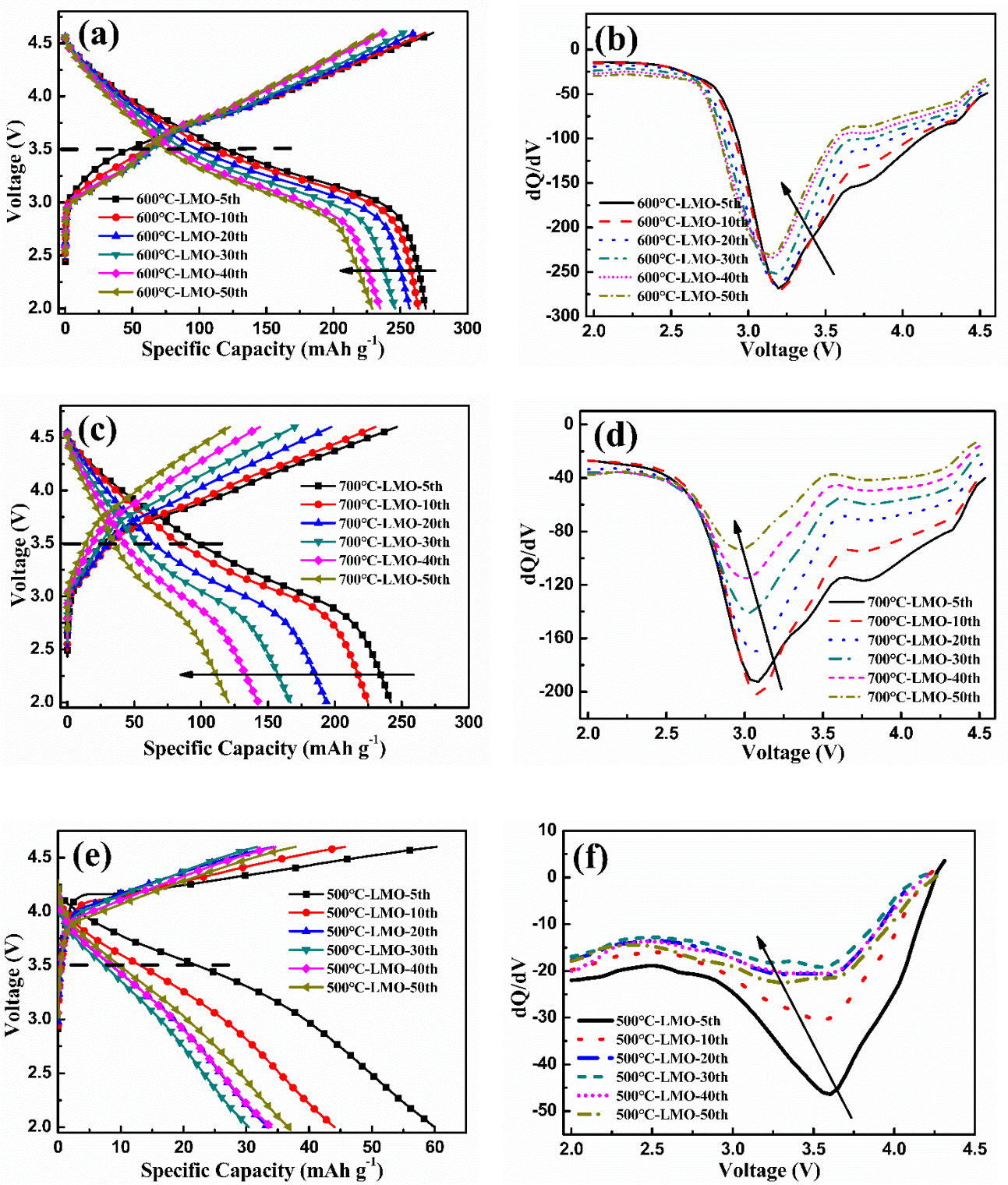

Figure 6. (a, c, e) Discharge curves in different cycles at 0.1 C, (b, d, f) dQ/dV plots for LMO pre-treatment at different temperatures.

Meanwhile, the increase in polarization caused by changes in interface conditions and the dissolution of transition metal ions are both crucial causes of the negative voltage shift. Table 3 shows that the voltages of the 500℃-LMO, 600℃-LMO and 700℃-LMO materials are negatively shifted by 350, 50, and 100 mV after 50 cycles, indicating that the cycling stability of 600℃-LMO is better. Since the structure in the 600℃-LMO material is more stable, the voltage attenuation is suppressed.

The electrochemical impedance spectra (EIS) of the 500℃-LMO, 600℃-LMO and 700℃-LMO electrodes after the 5th, 10th, 20th, 30th, 40th, and 50th cycles were measured (Fig. 8 (a) and Fig. 8 (b)). The state of charge was 4.3 V in the charged state, and the test frequency range was 10 mHz~100 kHz. The equivalent circuit diagram for AC impedance fitting is shown in Fig. 7.

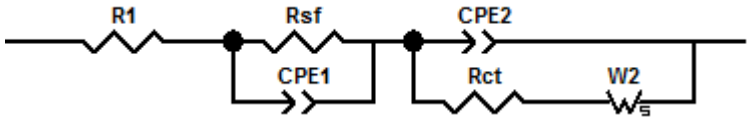

Figure 7. Equivalent circuit diagram of EIS

As shown in Fig. 8 (a), the Nyquist plot of the 600℃-LMO material has two semicircular arcs in different cycles, corresponding to the interface impedance (Rsf) and the charge transfer resistance (Rct). Comparing the fitting results in Tables 4, 5, and 6, it can be seen that the 600℃-LMO material has the lowest charge transfer resistance, suggesting that the 600℃-LMO material has a higher electrochemical reaction activity, which is mainly due to the presence of a spinel phase with a three-dimensional Li^+ transport channel in the material promoting the occurrence of an electrochemical reaction, which corresponds to the above electrochemical performance. In comparison, the interface impedance and charge transfer impedance of the 500℃-LMO material are very different. The very large charge transfer impedance and interface impedance indicate that 500℃-LMO has low electrochemical activity and that the dense thick SEI film affects the occurrence of electrochemical reactions, which is also the reason for the poor electrochemical performance of 500℃-LMO.

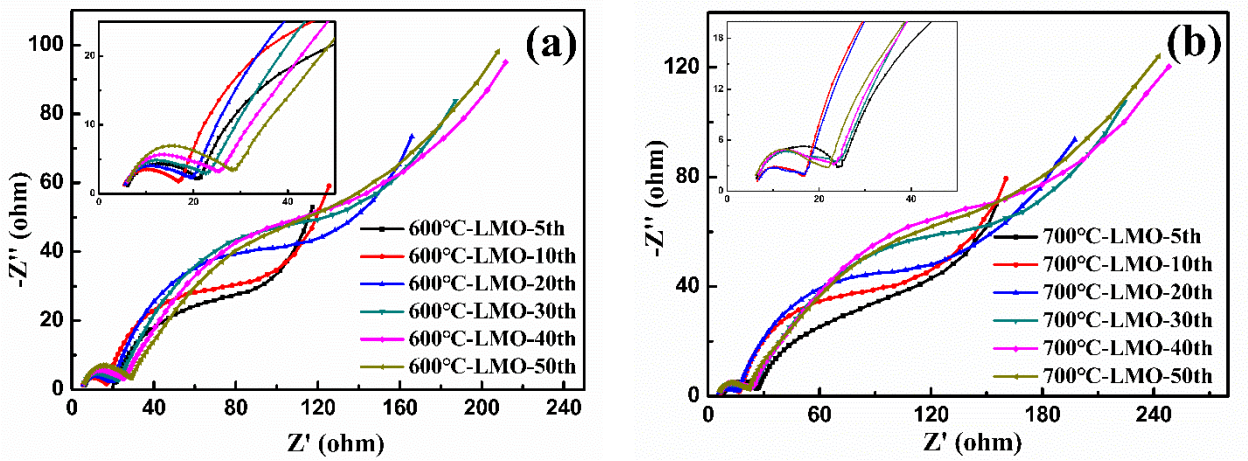

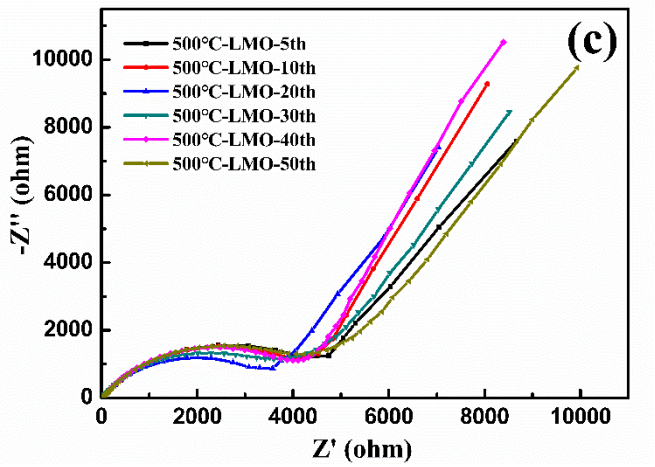

Figure 8. Nyquist plots of (a) 600℃-LMO, (b) 700℃-LMO and (c) 500℃-LMO after the 5th, 10th, 20th, 30th, 40th, and 50th cycles

Table 4. Fitted results of the EIS of 600℃-LMO

	5th	10th	20th	30th	40th	50th
R_Ω ($\Omega \cdot cm^2$)	7.84	6.51	6.38	6.78	7.07	7.68
R_{sf} ($\Omega \cdot cm^2$)	24.55	19.79	23.98	27.87	30.60	33.99
R_{ct} ($\Omega \cdot cm^2$)	27.84	104.09	158.77	224.84	254.41	265.03

Table 5. AC impedance fitting results of 700℃-LMO

	5th	10th	20th	30th	40th	50th
R_Ω ($\Omega \cdot cm^2$)	7.79	8.09	6.59	7.07	7.62	7.55
R_{sf} ($\Omega \cdot cm^2$)	31.92	18.20	19.00	29.51	26.32	23.61
R_{ct} ($\Omega \cdot cm^2$)	87.04	113.61	149.00	286.13	306.92	370.83

Table 6. AC impedance fitting results of 500℃-LMO

	5th	10th	20th	30th	40th	50th
R_Ω ($\Omega \cdot cm^2$)	10.73	9.70	9.35	9.63	9.72	10.80
R_{sf} ($\Omega \cdot cm^2$)	276.43	270.89	110.17	68.65	180.33	126.39
R_{ct} ($\Omega \cdot cm^2$)	6489.56	6176.94	5168.24	6032.18	6124.58	6791.40

To further analyse the structural changes of the 600℃-LMO and 700℃-LMO materials during cycling, XRD tests were performed on pole pieces of the 600℃-LMO and 700℃-LMO materials at 0.1 C for different cycle times. The test results are shown in Fig. 9. It can be seen from Fig. 9 (a) that the XRD diffraction peaks of the powder 600℃-LMO and the uncycled pole piece basically coincide, and the superlattice structure appears at 20°~25°. The superlattice structure disappears as the cycling progresses, which is mainly because Li_2O is removed from Li_2MnO_3 during the first charging process, forming a MnO_2 phase, and lithium is intercalated, forming $LiMnO_2$, during the discharge process; thus, the superlattice structure disappears. The XRD test structure verifies this process. After 30 cycles at 0.1 C, the XRD test structure of the pole piece shows that the R-3m structure is still maintained, no

new strong peaks appear, and there is no large shift in the position of the main peak, indicating that the material structure is stable and no structural changes occur. The XRD patterns of the 700℃-LMO material in Fig. 9 (b) are similar to those of 600℃-LMO, but as the cycling progresses, the position of the main peak moves to a small angle. According to the Bragg diffraction formula, the layer spacing of the material increases as the cycling proceeds. The above structural changes make the cycling stability of the 700℃-LMO material worse than that of 600℃-LMO. At the same time, the XRD test shows that there are no obvious new peaks in 700℃-LMO, and the specific structural changes require more elaborate characterization.

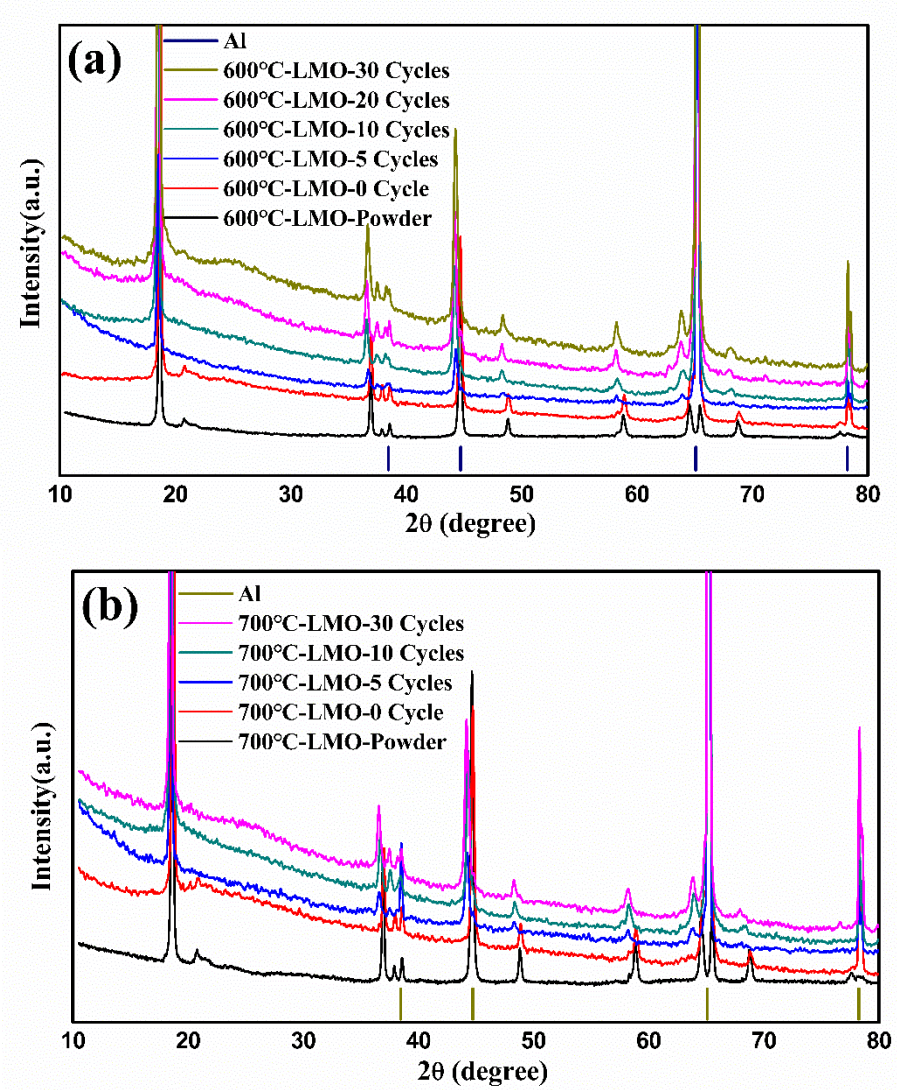

Figure 9. XRD patterns of the electrode after different cycles. (a) 600℃-LMO, (b) 700℃-LMO.

4. CONCLUSION

In this paper, 500℃-LMO, 600℃-LMO and 700℃-LMO lithium-rich materials were prepared by changing the pre-treatment temperature, and the morphology and structure of the materials were characterized using XRD, SEM and SAED. The phase composition of the metal oxide changes after changing the pre-treatment temperature. The valence state of the metal oxide pre-treatment at 600℃ is

the mixed valence state, and the lithium-rich material prepared after sintering mixed lithium has a monoclinic layered-hexagonal layered-cubic spinel composite structure. The initial specific discharge capacities of the 500℃-LMO, 600℃-LMO and 700℃-LMO materials are 136.3, 252 and 224 mAh g^{-1}, respectively, and the Coulombic efficiencies are 56.1%, 81.4% and 73.8%. The 600℃-LMO material has a specific discharge capacity of 183 mAh g^{-1} at 300 mA g^{-1}, while the 700℃-LMO and 500℃-LMO materials only have values of 148 and 17 mAh g^{-1}. The differences in the performance are due to the presence of the spinel phase, which provides a three-dimensional transport channel in the layered material, ensuring the rapid intercalation and decoupling of Li^+ with large performance enhancement.

ACKNOWLEDGEMENTS
This work was financially supported by the Science and Technology Program of the State Grid Corporation of China (Program Title: Development of low cost and high safety lithium ion battery based on manganese series).

References

1. J. Lee, D.A. Kitchaev, D.H. Kwon, C.W. Lee, J.K. Papp, Y.S. Liu, Z. Lun, R.J. Clement, T. Shi, B.D. McCloskey, J. Guo, M. Balasubramanian, G. Ceder, *Nature*, 556 (2018) 185.
2. P.K. Nayak, E.M. Erickson, F. Schipper, T.R. Penki, N. Munichandraiah, P. Adelhelm, H. Sclar, F. Amalraj, B. Markovsky, D. Aurbach, *Adv. Energy Mater.*, 8 (2018) 1702397.
3. G.X. Wang, J.H. Ahn, J. Yao, S. Bewlay, H.K. Liu, *Electrochem. Commun.*, 6 (2004) 689.
4. J.L. Shi, D.D. Xiao, M. Ge, X. Yu, Y. Chu, X. Huang, X.D. Zhang, Y.X. Yin, X.Q. Yang, Y.G. Guo, L. Gu, L.J. Wan, *Adv. Mater.*, 30 (2018) 1705575.
5. N. Nitta, F. Wu, J.T. Lee, G. Yushin, *Mater. Today*, 18 (2015) 252.
6. W. Song, J. Liu, L. You, S. Wang, Q. Zhou, Y. Gao, R. Yin, W. Xu, Z. Guo, *J. Power Sources*, 419 (2019) 192.
7. M. Nanthagopal, P. Santhoshkumar, N. Shaji, S. Praveen, H.S. Kang, C. Senthil, C.W. Lee, *Appl. Surf. Sci.*, 492 (2019) 871.
8. M.H. Pyun, Y.J. Park, *J. Alloy. Compd.*, 643 (2015) S90.
9. H. Yu, H. Zhou, *J. Phys. Chem. Lett.*, 4 (2013) 1268.
10. W. Hua, S. Wang, M. Knapp, S.J. Leake, A. Senyshyn, C. Richter, M. Yavuz, J.R. Binder, C.P. Grey, H. Ehrenberg, S. Indris, B. Schwarz, *Nat. Commun.*, 10 (2019) 5365.
11. W. Jiang, C. Yin, Y. Xia, B. Qiu, H. Guo, H. Cui, F. Hu, Z. Liu, *ACS Appl. Mater. Interfaces*, 11 (2019) 14023.
12. S. Sharifi-Asl, V. Yurkiv, A. Gutierrez, M. Cheng, M. Balasubramanian, F. Mashayek, J. Croy, R. Shahbazian-Yassar, *Nano Lett.*, 20 (2019) 1208.
13. N. Li, S. Hwang, M. Sun, Y. Fu, V. S. Battaglia, D. Su, W. Tong, *Adv. Energy Mater.*, 9 (2019) 1902258.
14. Z. Zhu, D. Yu, Y. Yang, C. Su, Y. Huang, Y. Dong, I. Waluyo, B. Wang, A. Hunt, X. Yao, J. Lee, W. Xue, J. Li, *Nature Energy*, 4 (2019) 1049.
15. P. Liu, H. Zhang, W. He, T. Xiong, Y. Cheng, Q. Xie, Y. Ma, H. Zheng, L. Wang, Z. Zhu, Y. Peng, L. Mai, D. Peng, *J. Am. Chem. Soc.*, 141 (2019) 10876.
16. P.K. Nayak, J. Grinblat, M. Levi, E. Levi, S. Kim, J.W. Choi, D. Aurbach, *Adv. Energy Mater.*, 6 (2016) 1502398.
17. S. Yang, P. Wang, H. Wei, L. Tang, X. Zhang, Z. He, Y. Li, H. Tong, J. Zheng, *Nano Energy*, 63 (2019) 103889.
18. Y. Ma, P. Liu, Q. Xie, G. Zhang, H. Zheng, Y. Cai, Z. Li, L. Wang, Z. Zhu, L. Mai, D. Peng, *Nano*

Energy, 59 (2019) 184.
19. K. Mu, Y. Tao, Z. Peng, G. Hu, K. Du, Y. Cao, *Appl. Surf. Sci*., 495 (2019) 143503.
20. Z.Y. Yu, J. Liu, Z. Wang, W.J. Li, J.S. Hao, H.X. Liu, *Int. J. Electrochem. Sci.*, 14 (2019) 4216.
21. J. Yuan, J.W. Wen, J.B. Zhang, D.M. Chen, D.W. Zhang, *Electrochim. Acta*, 230 (2017) 116.
22. C.k. Song, W.J. Feng, W.X. Su, L.J. Chen, M.M. Li, *Int. J. Electrochem. Sci.*, 14 (2019) 2372.
23. M.M. Thackeray, S.H. Kang, C.S. Johnson, J.T. Vaughey, S.A. Hackney, *Electrochem. Commun.*, 8 (2006) 1531.
24. D.K. Lee, S.H. Park, K. Amine, H.J. Bang, J. Parakash, Y.K. Sun, *J. power Source.*, 162 (2006) 1346.
25. G.Y. Kim, S.B. Yi, Y.J. Park, H.G. Kim, *Mater. Res. Bull.*, 43 (2008) 3543.
26. A.D. Tang., K.L. Huang. *Mater. Chem. Phys.*, 93 (2005) 6.
27. D.Z. He, Q.X. Guo, H. Yin, J.T. Li, Z.L. Gong, *Int. J. Electrochem. Sci.*, 12 (2017) 455.
28. M.G. Kim, M. Jo, Y.S. Hong, J. Cho, *Chem. Commun.*, 2 (2009) 218.
29. J.H. Liu, H.Y. Chen, J.N. Xie, Z.Q. Sun, N.N. Wu, B.R. Wu, *J. Appl. Electrochem.* 44 (2014) 225.
30. Y.T. Zhang, P.Y. Hou, E. Zhou, X.X. Shi, X.Q. Wang, D.W. Song, J. Guo, L.Q. Zhang, *J. Power Sources*, 292 (2015) 58.
31. B. Qiu, C. Yin, Y.G. Xia, and Z.P. Liu, *ACS Appl. Mater. Inter.*, 9 (2017) 3661.
32. L. Wang, Z. Wang, F. Yu, B. Liu, Y. Zhang, Y. Zhou, *Ceram. Int.*, 42 (2016) 14818.
33. L. Nation, Y. Wu, C. James, Y. Qi, B.R. Powell, B.W. Sheldon, *J. Mater. Res.*, 33 (2018) 4182.
34. Q. Xia, X. Zhao, M. Xu, Z. Ding, J. Liu, L. Chen, D. G. Ivey, W. Wei, *J. Mater. Chem. A*, 3 (2015) 3995.
35. Y. Pei, C.Y. Xu, Y.C. Xiao, Q. Chen, B. Huang, B. Li, S. Li, L. Zhen, G.Z. Cao, *AFM*, 27 (2017) 1604349.
36. K.H. Nie, X.R. Sun, J.Y. Wang, Y. Wang, W.B. Qi, D.D. Xiao, J.N. Zhang, R.J. Xiao, X.Q. Yu, H. Li, X.J. Huang, L.Q. Chen, *J. power sources*, 470 (2020) 228423.
37. N. Srivastava, S.K. Singh, H. Gupta, D. Meghnani, R. Mishra, R.K. Tiwari, A. Patel, A. Tiwari, R.K. Singh, *J. Alloys Compd*, 843 (2020) 155615.
38. Z.G. Tai, W. Zhu, M. Shi, Y.F. Xin, S.W. Guo, Y.F. Wu, Y.Z. Chen, Y.N. Liu, *J. Colloid Interface Sci.*, 576 (2020) 468.